CHEMISTRY OF MATERIALS
Cite This: Chem. Mater. 2019, 31, 1391−1402
Article
pubs.acs.org/cm

Remarkably Distinct Mechanical Flexibility in Three Structurally Similar Semiconducting Organic Crystals Studied by Nanoindentation and Molecular Dynamics

Ramesh Devarapalli,[†] Sourabh Bhagwan Kadambi,[‡,#] Chun-Teh Chen,[§] Gamidi Rama Krishna,[†,⊥] Bal Raju Kammari,[†] Markus J. Buehler,[*,§] Upadrasta Ramamurty,[*,‡,∥] and C. Malla Reddy[*,†]

[†]Department of Chemical Sciences, Indian Institute of Science Education and Research (IISER) Kolkata, Mohanpur Campus, Mohanpur 741 246, India

[‡]Department of Materials Engineering, Indian Institute of Science, Bangalore 560 012, India

[§]Laboratory for Atomistic and Molecular Mechanics (LAMM), Department of Civil and Environmental Engineering, Massachusetts Institute of Technology, 77 Massachusetts Avenue, Cambridge, Massachusetts 02139, United States

[∥]School of Mechanical and Aerospace Engineering, Nanyang Technological University, Singapore 639978, Singapore

Supporting Information

ABSTRACT: Distinct macroscopic mechanical responses of the three crystals of naphthalene diimide derivatives, **1Me**, **1Et**, and **1nPr**, studied here are very intriguing because their molecular structures are very similar, with the difference only in the alkyl chain length. Among the three crystals examined, **1Me** shows highly plastic bending nature, **1Et** shows elastic flexibility, and **1nPr** is brittle. A detailed investigation by nanoindentation and molecular dynamics (MD) simulations allowed us to correlate their distinct mechanical responses with the way the weak interactions pack in crystal structures. The elastic modulus (E) of **1Me** is nearly an order of magnitude lower than that of **1Et**, whereas hardness (H) is less than half. The low values of E and H of **1Me** indicate that these crystals are highly compliant and offer a low resistance to plastic flow. As the knowledge of hardness and elastic modulus of molecular crystals alone is insufficient to capture their macroscopic mechanical deformation nature, that is, elastic, brittle, or plastic, we have employed three-point bending tests using the nanoindentation technique. This allowed a quantitative evaluation of flexibility of the three mechanically distinct semiconducting molecular crystals, which is important for designing larger-scale applications; these were complemented with detailed MD simulations. The elastic **1Et** crystals showed remarkable flexibility even after 1000 cycles. The results emphasize that the alkyl side chains in functional organic crystals may be exploited for tuning their self-assembly as well as their mechanical properties. Hence, the study has broad implications, for example, in crystal engineering of various flexible, ordered molecular materials.

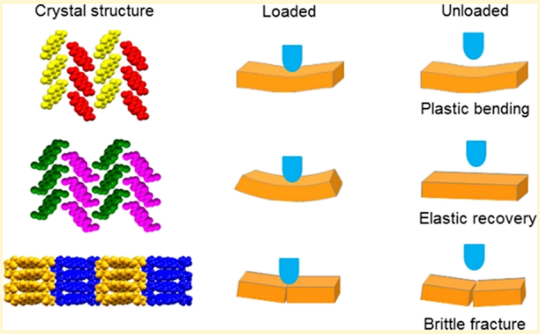

INTRODUCTION

Relatively dense packing combined with a high structural order (as compared to less-ordered organic solids) make organic single crystals excellent candidates for applications involving electron transport, rapid mechanical actuation, and so forth.[1−13] However, most of them are fragile and are inferior to thin films and liquid crystals in terms of mechanical flexibility, which is vital for high-performance modular organic microelectronics of the future.[14,15] Recently, applications of flexible organic crystals have been notably studied in waveguides,[10,11] ferroelectricity,[12] field-effect transistors for ultrasensitivity strain sensing,[13] and so forth. In view of the unique advantages offered by high-quality single crystals in certain applications, there have been attempts to achieve solution-processable micropatterns on flexible substrates by controlling the crystal growth.[16−18] Mechanical durability of semiconducting thin films deposited on flexible substrates is well-studied,[19,20] but there are only a few studies with a focus on single crystals. Applications of large single crystals, with brittle and fragile nature, deposited on flexible substrates can pose challenges because of disintegration or development of severe defects under mechanical impact. Hence, there is an urgent need to systematically study the macroscopic mechanical deformability of semiconducting organic crystals and to emulate design methodologies by understanding their structure−property relationships.[21−27]

Most molecular crystals typically break when deformed, without exhibiting any notable flexibility on the macroscopic

Received: November 18, 2018
Revised: January 18, 2019
Published: January 23, 2019

DOI: 10.1021/acs.chemmater.8b04800
Chem. Mater. 2019, 31, 1391−1402

level.[28,29] Some, with low molecular energy surfaces formed by weak interactions, deform plastically, that is, irreversibly and readily, with the deformed material containing several defects; some of them can even become polycrystalline with a slight misorientation of the grains with respect to each other.[30,31] Certain molecular crystals exhibit a high degree of elasticity.[32−34] A cocrystal of caffeine and 4-chloro-3-dinitrobenzoic acid with methanol solvent was such an elastic molecular crystal that was first to be reported.[2] Certain Schiff bases with weak interactions were also shown to exhibit substantial elastic bendability.[34] This was attributed to structural features that allow some localized structural changes but restrict long-range slip of crystallographic planes past each other. The semiconducting organic single crystals with high mechanical flexibility remain unexplored, despite the immense interest in them for various applications.[35−38] For utilizing flexible semiconducting crystals for practical applications, it is vital to assess their macroscopic mechanical deformation in a quantitative manner. Although the elastic moduli (E) of many molecular crystals have been experimentally evaluated by employing the nanoindentation technique in recent years, they do not provide the necessary information about the mechanical flexibility of crystals. This is because E, which is given by the slope of the stress−strain response, only informs us about the resistance offered by a material to elastic deformation, whereas in many instances one would like to know the total elastic strain that it can accommodate before either deforming permanently or fracturing.

In this paper, the structural basis for elastic behavior of *N*,*N*′-diethyl-1,4,5,8-naphthalenetetracarboxylic diimide (**1Et**) is investigated and compared with those of two other naphthalene diimide (NDI) derivatives, *N*,*N*′-dimethyl-1,4,5,8-naphthalenetetracarboxylic diimide (**1Me**) and *N*,*N*′-din-propyl-1,4,5,8-naphthalenetetracarboxylic diimide (**1nPr**), which show markedly different mechanical responses, namely plastic and brittle behaviors. The three molecular structures differ only in the alkyl substitution and such a large difference in mechanical behavior is unanticipated from the current crystal engineering knowledge because the alkyl groups are considered to be innocent and play a minimal role, especially when the crystal structures are also very similar. The three NDIs with very close molecular similarity, comparable crystal packing, and nearly same crystal morphologies also gave us a unique opportunity to carry out detailed mechanical deformation studies for the first time on three diverse types, plastic, elastic, and brittle crystals, by bending tests using the nanoindentation technique to unravel their distinct mechanical responses. This was complimented by molecular dynamics (MD) simulations and energy framework analysis for deeper understanding of molecular level structural deformation. Hence, this study helps to understand the mechanical flexibility of not only semiconducting organic crystals but also other organic crystals such as active pharmaceutical ingredients, where the behavior of individual particles plays a key role in bulk properties, for example, in powder compaction, milling, and particle size distribution in industrial scale crystallization (which is influenced by particle disintegration during mixing by mechanical agitation).[39−42]

RESULTS AND DISCUSSION

Three NDI derivatives **1Me**, **1Et**, and **1nPr** with methyl, ethyl, and *n*-propyl alkyl groups, respectively, (Scheme 1) were prepared by reacting 1,4,5,8-naphthalenetetracarboxylic dianhydride (1) with the corresponding amines using the known procedures.[43] Crystals were obtained from either dichloromethane or chloroform solvent by the slow evaporation method under ambient conditions for 5 to 6 days, which yielded needlelike crystals that were ∼5 mm long and ∼0.5 × 1 mm^2 in cross-section. These crystals were amenable for both single-crystal X-ray diffraction (SCXRD) and mechanical property evaluation.

Scheme 1. Molecular Structures of the NDI Derivatives with Methyl (1Me), Ethyl (1Et), and *n*-Propyl (1nPr) Substituents Examined in This Study

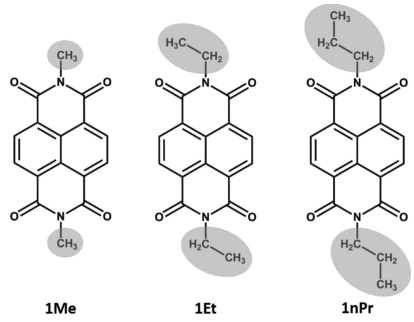

Crystal Structures. Crystallographic features of **1Me** and **1nPr** (except **1Et**) have been already reported in our recent work,[22] and hence they are described in brief here. **1Me** crystallizes in the monoclinic space group $P2_1/c$ with half a molecule in the asymmetric unit. The molecules pack into columns via π-stacking interactions along the *a*-axis. The adjacent columns are tilted in the opposite direction to form corrugation and connected via weak C(sp^2)−H···O (d/Å, θ/°; 2.409 Å, 153.07°) interactions. These stacked columns close-pack in the orthogonal direction via hydrophobic −Me groups to form weak interaction planes parallel to (0 0 1) (see Figure 1a). There are no other significant hydrogen-bond interactions in the structure.

Crystals of **1Et** also adapt the monoclinic space group $P2_1/c$ with half a molecule in the asymmetric unit. The overall packing resembles that of **1Me**. However, the alkyl groups in

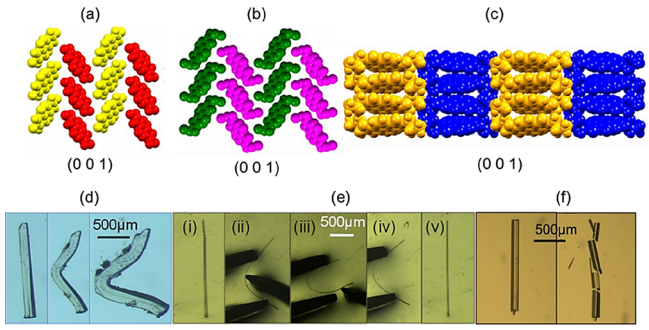

Figure 1. Crystal packing to show the topology of alkyl group-based weak interaction planes between π-stacked columns and the mechanical deformation behavior of the crystals. (a) Formation of slip planes by the close packing of Me groups in **1Me**. Corresponding planes in **1Et** (b) are interlocked because of the zigzag packing of Et groups. The *n*-Pr groups in **1nPr** (c) are moderately interlocked and face against each other. In all three cases, the weak interaction plane formed by alkyl groups is (0 0 1). (d−f) Microscopic images of plastic bending, elastic recovery, and brittle fragmentation of crystals of **1Me**, **1Et**, and **1nPr**, respectively, when their mechanical response is probed in a qualitative manner.

DOI: 10.1021/acs.chemmater.8b04800
Chem. Mater. 2019, 31, 1391−1402

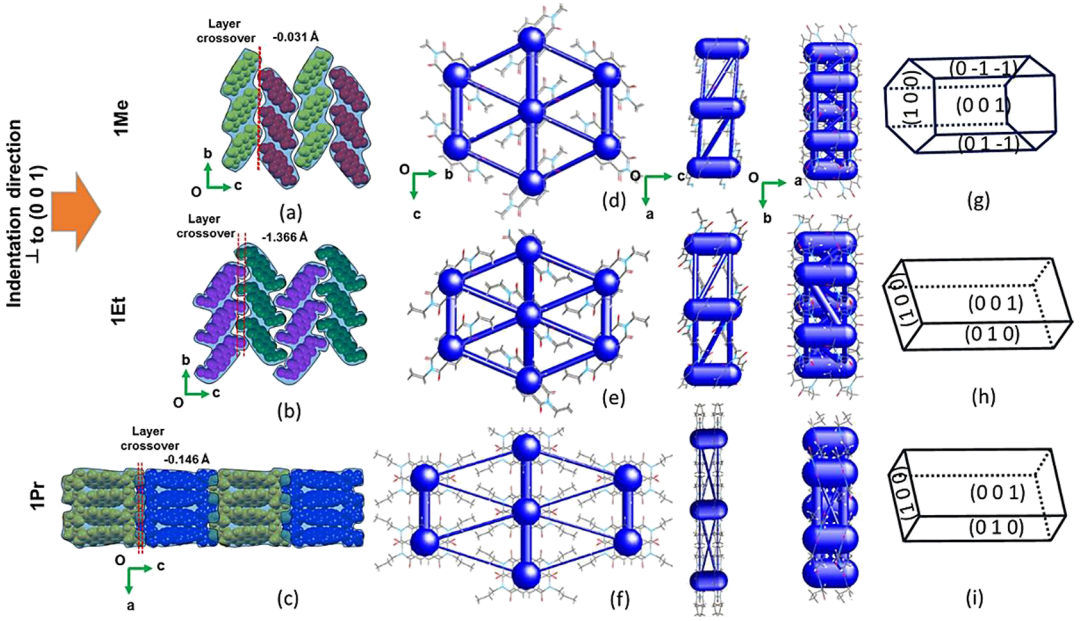

Figure 2. Representation of slip layer topologies, energy frameworks, and face indices of the three NDI derivatives. (a–c) are the packing views representing layer topologies (follow blue shade, particularly see at the slip plane) of **1Me**, **1Et**, and **1nPr**. Orange arrow on the left shows the indentation direction, whereas the red dotted lines indicate the cross-over distance of layers in slip planes. Different views of 3D topologies of energy frameworks (d–f) for **1Me** (plastic), **1Et** (elastic), and **1nPr** (brittle), respectively. Schematic representation of the face indices of crystals (g) **1Me**, (h) **1Et**, and (i) **1nPr**.

1Et close-pack in a zipper-type fashion with a crossover of −1.37 Å because of the elongated shape of the alkyl moiety bearing an extra methylene group (Figure 1b). This makes the alkyl plane considerably serrated as compared to that in **1Me** (Figure 1a). In the crystal packing, except the weak C(sp^2)−H···O (2.396 Å, 148.97°) interactions, no other significant short contacts are present.

The **1nPr** compound crystallizes in the orthorhombic space group *Pbca* with one molecule in the asymmetric unit. In this case also, the aromatic groups form π-stacked molecular columns along the *a*-axis, but the overall packing is significantly different from those of **1Me** and **1Et**. The adjacent stacks are close-packed with propyl···propyl hydrophobic interactions. Unlike in **1Me** and **1Et**, the adjacent molecules in a stack here are rotated with respect to each other at an angle of 53.66° (see Supporting Information, Figure S1). As a result, the elongated *n*-Pr ($-CH_2-CH_2-CH_3$) groups between the adjacent stacked columns face against each other with some degree of interlocking, contrary to spherical −Me in **1Me** (Figure 1c). Hence, the topology of the corresponding weak interaction plane in this case is considerably different.

Qualitative Mechanical Tests. The mechanical responses of **1Me**, **1Et**, and **1nPr** were first examined qualitatively by pushing the long acicular single crystals with a metal needle from one side while holding the ends with a pair of forceps. The crystals of **1Me** exhibit plasticity readily, that is, when the force was applied on the (0 0 1) face of the crystal, a permanent deformation was observed with no visible recovery upon unloading (Figure 1d). The crystals broke, when the force was applied on the other pair of faces (0 1 −1) and (0 −1 −1) under similar conditions. Thus, plastic deformation is anisotropic and orientation-dependent.

In complete contrast, the crystals of **1Et** exhibit impressive elastic flexibility, that is, the crystal regains its original shape without any loss of morphological integrity upon unloading (Figure 1e). It is worth noting that only a few such elastic molecular crystals are reported in the literature.[32−38,44−48] Ghosh et al. reported some crystals of organic imines with a high degree of elastic deformation and suggested that the presence of multitude of weak intermolecular interactions and corrugated packing of stacked molecules is responsible for such behavior.[2,32−34] Whereas the former feature renders it easy for the sliding of molecules, the latter prevents long-range layer sliding, which would otherwise lead to a permanent change of shape. As described earlier, both these features are present in **1Et** crystals; the aromatic NDI groups close-pack via π-stacking, whereas the ethyl groups from adjacent stacks are arranged in a zipper-type fashion.

Crystals of the third compound **1nPr** are brittle, that is, they fragment readily, irrespective of the face on which the force was applied (Figure 1f and Figure S2, Supporting Information).

Energy Frameworks. Quantification of intermolecular interaction energies is carried out from the energy framework analysis (using CrystalExplorer, 17.5) to rationalize the observed mechanical behavior of the crystals.[49−51] The magnitude of calculated energies between molecular pairs are represented as cylinders of proportionate thickness joining the centers of mass (Figure 2). As visualized from the three-dimensional (3D) topologies of energy frameworks of **1Me** and **1Et** (Figures S3 and S4, Supporting Information), each molecule is surrounded by 12 closest neighbors: two within the stacked column, two between columns, and eight across alkyl slip planes. In the case of **1nPr** (Figure S5, Supporting Information), each molecule is surrounded by 14 neighbors, with two in the stacked column, six across alkyl planes, and six in between columns. The aggregate of total energies were considered separately for (i) stacked columns, (ii) inter-column, and (iii) alkyl slip plane. This representation revealed that the main structural feature in all cases is the strong π-

DOI: 10.1021/acs.chemmater.8b04800
Chem. Mater. 2019, 31, 1391−1402

Table 1. Average Mechanical Properties, Elastic Modulus, and Hardness, Estimated from Nanoindentation Tests, and Bending Modulus, Determined from Three-Point Bending Tests, and Aggregate Values of Total Intermolecular Interaction Energies for the Tape, Stacking, and Alkyl Slip Plane, Calculated Using Energy Frameworks for 1Me, 1Et, and 1nPr Crystals

Crystal	Indentation face	Elastic modulus, E (GPa)	Hardness, H (MPa)	Bending modulus, E_b (GPa)	% Elastic Strain	Layer separation (+)/ crossover (-) in Å	Aggregate of total interactions energies (kJ/mol)		
							Stack	Tape	Slip plane
1Me (Plastic)	Major (0 0 1)	1.82 ± 0.10	223 ± 7	1.83 ± 0.37	0.8	-0.031	-122	-47	-75
	Minor (0 1 -1) or (0 -1 -1)	-	-	3.76					
1Et (Elastic)	Major (0 0 1), Minor (0 1 0)	16.10 ± 0.44	502 ± 38	3.58 ± 0.67	1.6	-1.366	-127	-50	-99
1nPr (Brittle)	Major (0 0 1)	8.49 ± 0.09	399 ± 7	2.51 ± 0.34	0.4 - 0.8	-0.146	-158	-92	-40
	Minor (0 1 0)	10.18 ± 0.24	427 ± 22	-					

Scheme 2. Assessment of the Mechanical Behavior of Crystals by Nanoindentation Technique[a]

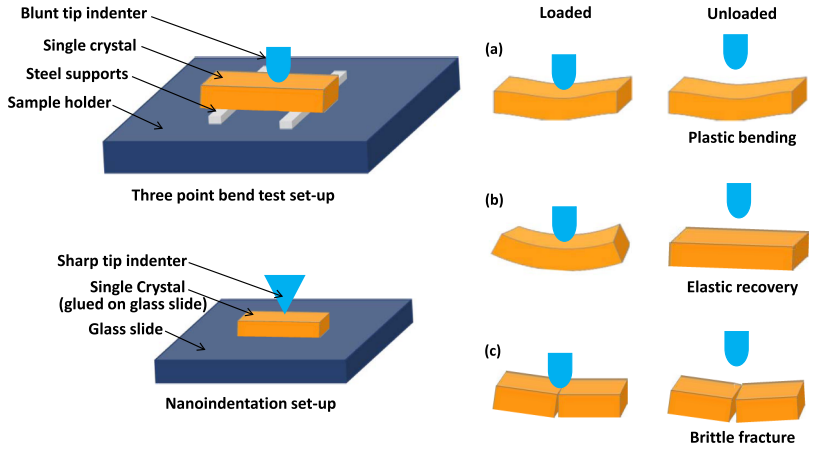

[a](Top left) Schematic setup showing the mounting of a sample for three-point bending tests on three types of crystals using a nanoindenter. Schematic representation of (a) plastic, (b) elastic, and (c) brittle mechanical responses observed in crystals of **1Me**, **1Et**, and **1nPr**, respectively. The inset (bottom left) shows the regular indentation setup where the crystal is glued directly on the sample substrate (glass slide) without steel supports for measuring the hardness and elastic modulus of the crystals.

stacked column along [1 0 0], with total interaction energies of −122, −127, and −158 kJ mol^{-1} for **1Me**, **1Et**, and **1nPr**, respectively (Table 1). In the first two, the energies corresponding to the slip plane are moderate (−75 and −99 kJ mol^{-1}, respectively), whereas the intercolumn interactions are the lowest (−47 and −50 kJ mol^{-1}, respectively). Although the intercolumn interaction energies in **1Me** (−47 kJ mol^{-1}) and **1Et** (−50 kJ mol^{-1}) are the lowest, the possibility of slip occurring along these planes in **1Me** and **1Et** can be ruled out because of the highly corrugated nature of the molecular packing on these planes (Figure 2). Hence, in **1Me**, the plane formed by methyl groups is likely to be the facile slip plane, allowing for long-range shear sliding that facilitates macroscopic plasticity. In the case of **1Et**, the ethyl groups cross over the plane by −1.37 Å, leading to interlocking, and hence slip on (0 0 1) is difficult. Whereas such topological interlocking of molecules can arrest long-range sliding of the molecular planes, it may allow for smaller localized molecular displacements, that is, tilting of molecules associated with slight expansion or contraction of intermolecular space. In the case of **1nPr**, the aggregate of total energies for the alkyl slip plane is the lowest (−40 kJ mol^{-1}) and intercolumn energies are moderate (−92 kJ mol^{-1}). In this case, slip parallel to the alkyl plane is not possible as the propyl groups are faced against each other with a moderate layer cross-over of −0.146 Å. Although the molecules perpendicular to the stacking have a separation of 1.64 Å in (1 0 0), the large stacking energy (−158 kJ mol^{-1}) in **1nPr** probably makes the stacks rigid, preventing plastic bending in the crystals. The brittle **1nPr** also has a much shorter stacking distance of 3.5 Å compared to **1Me** (4.6 Å) and **1Et** (4.8 Å) (Figure S2, Supporting Information). Hence, crystals of the former can neither accommodate elastic nor plastic deformation and hence are brittle.

Quantitative Mechanical Tests. The mechanistic inferences about the causes for the distinctly different mechanical responses of the three compounds made above were further substantiated through quantitative mechanical probing by the nanoindentation technique[3] as well as MD simulations. Nanoindentation experiments were utilized to measure the elastic modulus (E) and hardness (H) in different orientations of the single crystals (mounted on a flat surface, Scheme 2, inset). Crystals were also deformed in the three-point flexure

DOI: 10.1021/acs.chemmater.8b04800
Chem. Mater. 2019, 31, 1391−1402

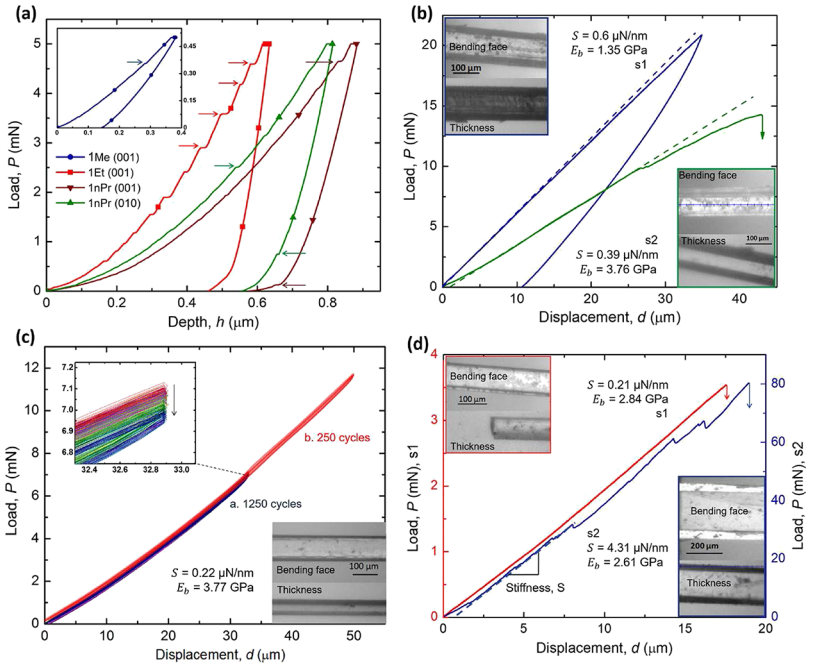

Figure 3. Load−displacement, $P-d$, curves obtained from different modes of nanoindentation experiments. (a) Representative load−depth ($P-h$) curves obtained from nanoindentation on **1Me** (shown in inset), **1Et**, and **1nPr** crystals. The $P-h$ curves shown for **1Me** and **1Et** correspond to the crystal's major face and those shown for **1nPr** correspond to the crystal's major (brown color) and minor (green color) faces. Arrows pointing to the right indicate the presence of "pop-in" in the loading segment and those pointing to the left indicate the occurrence of "pop-out" in the unloading segment of the curves. (b) $P-d$ curves obtained through 3PF tests of **1Me** with loading on the major (s1) and the minor (s2) faces. Note that s1 shows a remnant displacement after unloading, whereas s2 serration shows features indicative of plastic deformation followed by fracture. (c) Cyclic $P-d$ curves of **1Et** loaded to 1250 cycles, with a maximum displacement, h_{max}, fixed at 35 μm in each cycle, and then loaded to 250 cycles, with h_{max} of 50 μm in each cycle. The curves show complete shape recovery during unloading, indicating high elasticity of the sample. The inset shows the drop in peak load, P_{max}, for consecutive cycles. Providing sufficient time gap between cycles allows recovery of P_{max} in the subsequent cycle. (d) $P-d$ curves of **1nPr** samples on different faces exhibit fracture during loading. In all panels, the dashed lines represent a linear fit to the initial linear portion of the loading segment. S and E_b denote the bending stiffness and bending modulus, respectively. Insets in all panels show optical images of the samples' faces and are labeled as "bending face" and "thickness" to indicate the faces perpendicular and parallel to the indenter motion (direction of the applied bending load), respectively. All 3PF tests were performed at a displacement rate of 2 μm/s.

(3PF) configuration to ascertain their elasto-plastic behavior (Scheme 2, top left). In these, the crystals were first placed on two supports with a predetermined separation distance (or the inner span, L) and then were pushed from top at the middle of the span using a spherical (blunt) tip. Given that the crystals are extremely small, conducting such tests on the macroscale is not possible. The ability of the nanoindenter to measure load, P, and displacement, h, on small scales and with high resolution was exploited here.

Representative load (P) versus depth of penetration (h) responses obtained through nanoindentation on the different crystal facets of the three different samples are shown in Figure 3a. In all cases, the peak load, P_{max}, is 5 mN, except for **1Me** where a lower P_{max} of 0.5 mN was used in view of its extreme softness (a representative $P-h$ response is displayed in the inset of Figure 3a). Indentations on the major and minor faces of **1Et** resulted in near-identical $P-h$ responses, and hence only one of them is shown. These $P-h$ responses also exhibit prominent serrations (or "pop-ins"), whereas those obtained on other crystals are relatively smooth. The standard Oliver-Pharr method is used for estimating the average values of E and H from the $P-h$ responses (Table 1). Note that while E is a measure of the resistance offered by the solid to elastic deformation, H measures the resistance to plastic deformation.

The following observations can be made from the data in Table 1. (a) Among the three crystals examined, **1Me** has the lowest E and H. In fact, its E is nearly an order of magnitude lower than that of **1Et**, whereas H is less than half. These indicate that **1Me** crystals offer low resistance to both elastic and plastic deformations. Our attempts to indent on (0 1 1) were not successful because this direction is nearly parallel to the slip plane, hence even softer, which did not allow for any meaningful measurements to be made. These observations are in excellent agreement with the anisotropic nature of the packing and plastic bending of the crystals observed in the qualitative deformation tests. (b) The identical indentation responses obtained on the major and minor faces of **1Et** reflect the isotropic response from the structure within this crystal. Although the overall packing in **1Et** is similar to **1Me**, the mechanical behavior differs significantly, which is a reflection of the importance of mechanical interlocking of the van der Waal groups. The uneven weak interaction plane with the zipper-type arrangement of the Et groups in the former (vs smooth planes in **1Me**) prevents slippage of molecules. Hence, the crystals of **1Et** show an isotropic response, whereas **1Me** is anisotropic. The crystals of **1nPr**, in contrast, exhibit a reasonable degree of anisotropy, with the minor face (0 1 0) showing slightly higher E and H as compared to the major face (0 0 1).

The observed mechanical properties in the three crystals, especially their relative order in terms of E and H, can be rationalized with the help of crystal packing with respect to indentation direction, as shown in Figure 2. Energy frameworks and topology analysis suggest that (0 0 1) is the

DOI: 10.1021/acs.chemmater.8b04800
Chem. Mater. 2019, 31, 1391−1402

potential slip plane in both **1Me** and **1Et**. However, the mechanism of deformation can be expected to be different when indentation is performed on this face of **1Me** and **1Et** (see MD simulations results below). E of **1Et** is nearly double that of **1nPr**. The higher E of **1Et** suggests that the zipper-type interlocking of weakly interacting ethyl groups offers significant resistance for localized displacement of molecules. The comparatively lower E of **1nPr** is possibly due to the moderate cross-over of alkyl groups and the difference in the orientation of molecules in the two structures with respect to the indentation direction. Although it is perpendicular to the alkyl plane in both the cases, the lower corrugation of molecules in **1nPr** eases the movement of molecules in the indentation direction (see Figure 2c). The lower H of the minor face than the major face of **1nPr** can be attributed to the arrangement of the alkyl slip plane parallel to the indentation direction (Figure 2).

The difference in the deformation behavior of the three crystals is also evident via the number of displacement bursts or "pop-ins" observed during the loading segment of nanoindentation. For instance, pop-ins are prominent in **1Et**'s $P-h$ responses. In comparison, the $P-h$ responses of **1Me** and **1nPr** are relatively smooth, which imply a continuous sliding of the molecular layers in response to the applied stress. Pop-ins in **1Et** can be attributed to a greater resistance to sliding and build up and then a sudden release of stress. The underlying mechanism could be the compression of stacked columns followed by rearrangement of layers or breaking of the molecular stacks.[3] (Note that pileup around indents, which generally accompanies pop-in events, was not observed in the scanning probe images). The unloading segment of the $P-h$ responses obtained on both (0 0 1) and (0 1 0) faces of **1nPr** crystals shows a unique "pop-out" feature, which indicates a sudden outward push of the indenter from the material. In general, "pop-outs" are caused because of the occurrence of reverse phase transformation or the formation of cracks in the material underneath the indenter during unloading.[52,53] The latter is the likely reason here as (a) the qualitative tests on **1nPr** clearly demonstrate it to be brittle and (b) phase transformation is not known in these crystals.

Representative load−displacement, $P-d$, responses obtained from 3PF tests on **1Me**, **1Et**, and **1nPr** crystals, carried out in the displacement control mode, are shown in Figure 3b−d, respectively. **1Me** crystals were loaded until a deviation from linearity was observed in the loading segment of the $P-d$ curve. They were subsequently unloaded to monitor the extent of permanent deformation. During unloading, the $P-d$ curve does not follow the loading segment to zero displacement but rather leaves a considerable residual deformation, indicative of high plasticity. The strain at the onset of plastic deformation (calculated using eq 2, Experimental Section), which is referred to as the yield strain (ε_y), is found to be 0.8% on an average (from 3 samples), whose $P-d$ curves showed a clear transition from the elastic to plastic region. This value is similar to ε_y of ∼0.5% typically reported in crystalline metals that undergo dislocation-mediated plasticity.

The **1Et** crystal was subjected to load−unload cycles with fixed maximum displacements (at the center of its span length), d_{max}, of either 30 or 50 μm in each cycle. In both the cases, the recorded loading curves were found to be nearly linear; the bending modulus, E_b, is calculated from the stiffness, S, which is taken as the slope of the linear fit to the initial part of the loading segment. On average (from 5 samples of **1Et**), E_b is found to be 3.58 GPa. Note that the modulus value reported here, which correlates with the ease of elastic deformation in bending, is significantly smaller compared to that (16.1 GPa) obtained from nanoindentation. After unloading, the $P-d$ curves revert to the zero point, indicating complete recovery and the highly flexible nature of **1Et**. At the applied maximum load and for the sample with thickness 54 μm considered here, analysis using simple bending mechanics reveals the maximum displacement to correspond to a maximum flexural strain, ε_{max}, of 1.6% (see eq 2, Experimental Section). This strain is the value at the midpoint of the span, directly below the applied load, and on the bottommost plane of the crystalline beam. Note that because of the limitation of the technique, the highest possible displacement at the yield or fracture point could not be reached. The applied strain here (which is the maximum testable value), from which **1Et** was still in the elastic region, is remarkable considering that most engineering materials such as metals and alloys yield plastically beyond only 0.5% strain. The observed elasticity up to a large strain in bending is of significance considering **1Et**'s potential applicability as a flexible organic semiconductor.

Furthermore, to assess **1Et**'s fatigue performance, the load−unload cycle, up to d_{max} = 30 μm and corresponding to ε_{max} = 1% (calculated using eq 2), was applied 1000 times without any time lag between each cycle. The results show excellent repeatability in the $P-d$ response and thus indicate the ability of the crystal to remain flexible. A slight drop, of less than 3%, in P_{max} (inset in Figure 3c) is observed at the end of cycling. However, further examination, by means of an additional 250 cycles, applied with a time gap (or lag) of 60 s after every 25 cycles (Figure 3c) shows the recovery of P_{max} to its original value on the cycle after the time interval. This suggests that the load drop observed previously was not due to a permanent structural change but rather due to delayed restoration response to the applied displacement or viscoelasticity, which was later observed to recover with time. Following this, the sample was subjected to a higher strain, ε_{max} = 1.6%, for 250 cycles. The results indicate excellent elastic nature and fatigue tolerance, both of which are critical to potential application scenarios of these materials.

The **1nPr** crystals, which exhibited brittle behavior in qualitative tests, were loaded in bending until fracture occurred. All samples failed at comparatively low displacements (less than 20 μm), corresponding to a failure strain of 0.4−0.8%. Below this strain, the $P-d$ responses show a linear elastic region and, when unloaded, recovered the deformation completely, a typical characteristic of a brittle material. Hence, the 3PF tests not only allowed us to evaluate the qualitative description of mechanical behavior but also to quantify the flexural strain in the plastic, elastic, and brittle crystals.

MD SIMULATION RESULTS

The connection between crystal structures and the observed mechanical behaviors is further examined by MD simulations on **1Me**, **1Et**, and **1nPr**. The crystal (unit cell) sizes of the three NDIs after MD equilibrations (shown in Table 2) are very close to our experimental measurements, indicating the suitability of the simulation setup and force field adopted in this study for investigating the structural properties of these NDIs.

On the basis of the Euler−Bernoulli beam theory, while a beam with a uniform cross-section is under a pure bending situation, a half of the cross-sectional area is under tension and

DOI: 10.1021/acs.chemmater.8b04800
Chem. Mater. 2019, 31, 1391−1402

Table 2. Comparison between the Unit Cell Sizes from Simulations and Experiments

crystal	a (Å) in silico	a (Å) expt.	b (Å) in silico	b (Å) expt.	c (Å) in silico	c (Å) expt.
1Me (plastic)	4.60	4.62	7.87	8.02	18.66	17.02
1Et (elastic)	5.02	4.84	7.66	7.74	19.88	18.32
1nPr (brittle)	7.54	6.96	16.99	17.24	28.14	27.58

the other half is under compression.[54] In this situation, if the bending moment keeps increasing, the beam typically will start to fail from the tensile side because the compressive strength of a material is generally higher than its tensile strength. Consequently, the tensile elastic limit (strain) of a material basically determines whether the material is brittle or flexible. In this study, tensile tests (see Simulations section) were performed to estimate the elastic limits of the three NDIs. The tensile stress−strain curves from the tensile tests are shown in Figure 4a. The stress in both **1Me** and **1Et** increases smoothly as the strain increases up to 10%. The result implies that both **1Me** and **1Et** have an elastic limit of at least 10%. However, the stress of **1nPr** drops to below zero at a strain of around 3%. The negative stress observed in the simulation suggests that **1nPr** becomes unstable as the crystal completely loses its tensile strength, indicating that its elastic limit is about 3%. Note that the perfect crystal structures used in theoretical estimates tend to provide much larger elastic limits than the observed experimental values because of the presence of defects in actual crystals. Thus, the estimated elastic limits of these NDIs cannot be directly compared to our experimental values. Nevertheless, the relative elastic limits of these NDIs in the simulations and experiments should be comparable. Hence, based on the simulation results, we conclude that the elastic limit of **1nPr** is much smaller compared to those of **1Me** and **1Et**. In addition, **1nPr** completely loses its tensile strength after passing its elastic limit, as evident from the sudden drop of the stress to below zero in the stress−strain curve (Figure 4a). This result indicates that **1nPr** is much brittle compared to **1Me** and **1Et**.

The estimated elastic moduli (calculated at ∼1% strain) of **1Me**, **1Et**, and **1nPr** in the simulations are 2.9, 6.3, and 10 GPa, respectively. Because the tensile tests in the simulations were performed in the [1 0 0] direction, the estimated elastic moduli are closer to the bending moduli (E_b) from our 3PF tests than the elastic moduli (E) from regular indentation tests. The result shows that NDIs with longer alkyl chain lengths should have higher elastic moduli, which explains why **1Me** has the smallest elastic modulus among these NDIs in our experiments.

However, the nanoindentation experiments show that the elastic modulus of **1nPr** is lower than that of **1Et**, and the opposite result is found in the simulations. This is possibly because **1nPr** is much brittle compared to **1Et**, and the nanoindentation measurement of **1nPr** might significantly damage the crystal because of cracking (which can propagate fast with the presence of defects in brittle crystals), leading to a smaller modulus than that of **1Et**. Pop-ins in the unloading curve of nanoindentation for **1nPr** further support this argument.

In addition to tensile tests, shear tests (see Simulations section) were performed to examine the plasticity of these NDIs. The shear stress−strain responses from these simulations are shown in Figure 4b, and the corresponding shear deformations are shown in Figure S7. To estimate the shear elastic limits of the three NDIs, unloading tests were performed at different amounts of shear strain, and the corresponding residual strains are shown in Table 3. After unloading at 3% shear strain, **1Me** has zero residual strain, showing that it is in the elastic region. However, as the applied shear strain is larger than its yield shear strain (∼4% as shown in Figure 4b), **1Me** becomes unstable as its shear modulus (the slope of the stress−strain response) becomes negative (see Figure 4b). **1Et** shows perfect elastic behavior after unloading at 3 and 10% shear strains, as it has a larger yield shear strain of ∼13% (see Figure 4b). Additionally, it was observed that the

Table 3. Residual Strains after Unloading at Different Amounts of Shear Strain

crystal	at 3%	at 10%	at 15%	at 20%	at 25%
1Me (plastic)	0.0				
1Et (elastic)	0.0	0.0	12.6	12.6	12.6
1nPr (brittle)	0.7	1.7	2.7	2.8	14.1

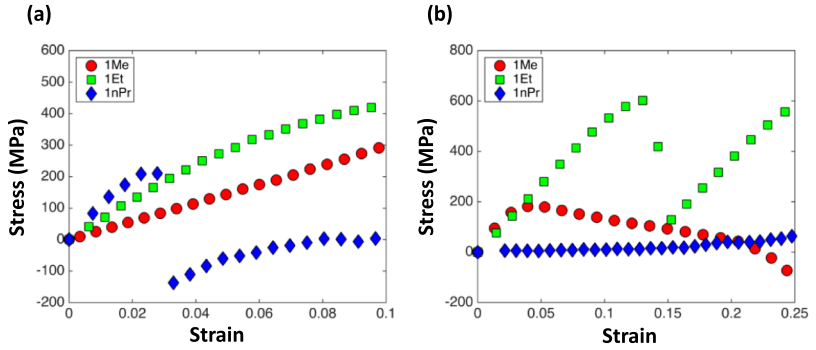

Figure 4. Tensile and shear test results from MD simulations. (a) Stress−strain curves from tensile tests in the [1 0 0] direction. The result shows that **1nPr** is much brittle compared to **1Me** and **1Et** because it has a much smaller elastic limit of ∼3% compared to the other two compounds with theoretical elastic limits of at least 10%. (b) Stress−strain curves from shear tests in the [1 0 0]−[0 0 1] direction. The result shows that the shear strength of **1Me** (∼200 MPa) is much lower than that of **1Et** (∼600 MPa). The yield shear strain of **1Me** (∼4%) is also much smaller than that of **1Et** (∼13%). As a result, **1Me** is much easier to deform plastically compared to **1Et**. **1nPr** has a much lower shear strength compared to **1Me** and **1Et**.

DOI: 10.1021/acs.chemmater.8b04800
Chem. Mater. 2019, 31, 1391−1402

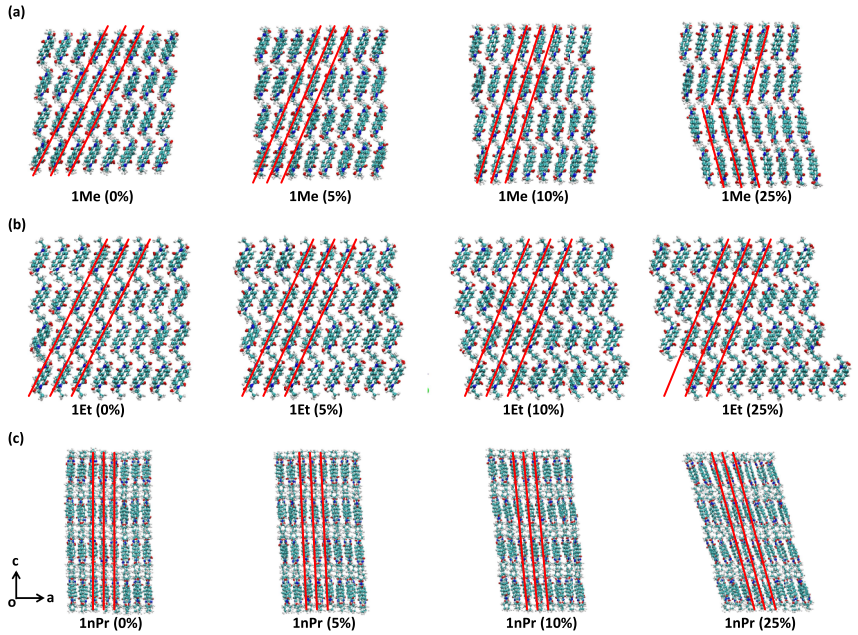

Figure 5. Detailed structural changes in crystal packing during shear tests carried out using MD simulations. (a–c) shows **1Me**, **1Et**, and **1nPr** during shear tests, respectively. The numbers in the brackets below the figures represent the corresponding shear strain. (Color code: cyan, carbon; blue, nitrogen; red, oxygen; and white: hydrogen).

plastic deformation in **1Me** is caused by twinning (probably due to the presence of low rugosity of slip planes and weaker stacking interactions, Figure 2a), whereas it occurs through slip in **1Et**. Although **1nPr** starts to show plastic behavior even at 3% shear strain, the residual strain obtained here is probably due to the extremely low shear modulus (see Figure 4b). In fact, after unloading at 20% shear strain, **1nPr** recovers 86% of the applied strain, showing that most of the deformation is still elastic. An obvious plastic behavior (14.1% residual strain) is only observed at 25% shear strain. Note that the shear strength of **1Me** (~200 MPa) is much lower than that of **1Et** (~600 MPa). Additionally, the yield shear strain of **1Me** (~4%) is much smaller than that of **1Et** (~13%). As a result, although both **1Me** and **1Et** show plasticity in the shear tests, **1Me** is much easier to deform plastically compared to **1Et**. This result explains why **1Me** behaved plastically and **1Et** behaved elastically in the experiments. Hence, the order of plasticity observed in the simulations is **1Me** > **1Et** > **1nPr**.

To understand how the crystal structures of **1Me**, **1Et**, and **1nPr** are related to their distinct mechanical behaviors, the structural changes in their crystal packing during the shear tests were examined in detail (Figure 5). In the case of **1Me** (Figure 5a), the angle of the slip planes with respect to the [1 0 0] direction changes from ~63.4° at zero shear strain to ~66.6° at 5% shear strain, ~72.3° at 10% shear strain, and ~74.7° at 25% shear strain. The simulation results show large movements of the molecules occurring during the shear tests, mainly because of the weak intermolecular interactions or, in other words, the presence of facile slip systems. The slip planes break into two parts at large strains (e.g., 25%), which cause the plastic deformation by twinning. In the case of **1Et**, the angle of the slip planes also changes as the shear strain increases (Figure 5b). The angle of the slip planes with respect to the [1 0 0] direction changes from ~63.4° at zero shear strain to ~65.6° at 5% shear strain, ~67.8° at 10% shear strain, and ~67.8° (the same as the angle at 10% shear strain) at 25% shear strain. It is noted that the changes are much less compared to the case of **1Me** (Figure 5a) because of the zipper-type interlocking and stronger stacking and intercolumn interactions (Figure S2, Supporting Information), which act as a hindrance to long-distance sliding of molecular layers. This greater resistance to sliding explains why the yield shear strain of **1Et** (~13%) is much larger than that of **1Me** (~4%) as well as why **1Me** behaved plastically and **1Et** behaved elastically in the experiments.

In the case of **1nPr**, the angle of the slip planes with respect to the [1 0 0] direction changes from ~90.0° at zero shear strain to ~92.6° at 5% shear strain, ~95.2° at 10% shear strain, and ~105.3° at 25% shear strain. **1nPr** has a much lower shear strength compared to **1Me** and **1Et** (see Figure 4b). Although twinning and slip are not observed in the shear tests, **1nPr** shows obvious plastic behavior at 25% shear strain. The lower H of **1nPr** compared to that of **1Et** in the nanoindentation tests is consistent with this observation (Table 1). However, whether **1nPr** can deform plastically or not does not change the fact that **1nPr** is much brittle compared to **1Me** and **1Et** because it has a much smaller elastic limit compared to the other two compounds (Figure 4a).

CONCLUSIONS

The qualitative mechanical deformation tests of three mechanically distinct types of NDI derivatives (**1Me**, **1Et**, and **1nPr**) quantified with exhaustive nanoindentation measurements, MD simulations, and energy framework analyses are presented in this study. Although the overall molecular structure and types of functional groups in **1Et**, **1Me**, and **1nPr** are comparable, the subtle differences in the way the alkyl groups are packed significantly influence their mechanical behaviors. Hence, controlling the mechanical properties of molecular crystals requires the understanding of not only the strength of intermolecular interactions but also their geometrical arrangement in the 3D packing (or topology of the molecular surface that forms the slip planes) as seen in this series. In this study, the crystals of **1Et** have been shown to

DOI: 10.1021/acs.chemmater.8b04800
Chem. Mater. 2019, 31, 1391–1402

be highly flexible with a yield strain of at least 1.6% compared to widely studied metals and alloys. MD simulations reveal that the deformation in plastic **1Me** is dominated by twinning, whereas it is slip in the elastic **1Et**. Certainly, this study demonstrates the importance of using the nanoindentation technique and full atomistic modeling to precisely quantify and predict the mechanical responses of macroscopic crystalline particles, which has implications for understanding the bulk behavior of crystalline powders.

EXPERIMENTAL SECTION

Materials. All reagents were purchased from Sigma-Aldrich. Commercially available solvents were used (for synthesis and crystallization) as received without further purification.

Synthesis. **1Me**, **1Et**, and **1nPr** were synthesized by condensation of the carboxylic acid dianhydride with two equivalents of the respective substituted amines in dimethylformamide at temperatures above 110 °C overnight.[43] All obtained compounds were purified by recrystallization and characterized by ^{1}H nuclear magnetic resonance (NMR) and single-crystal X-ray structure determination.

Single-Crystal Preparation. The three NDIs were recrystallized from either dichloromethane or chloroform solvent by slow evaporation under ambient conditions. Single crystals suitable for testing mechanical properties and for X-ray diffraction data were obtained in 5−6 days in all cases.

Single-Crystal X-ray Structure Determination. Intensity data of **1Et** was recorded on a Supernova (Eos CCD detector) diffractometer using monochromatic Mo Kα radiation (λ = 0.71073 Å). The data was collected at 100 K (same for all three NDIs). Using Olex^2,[55] the structure was solved with ShelXT and ShelXS (direct methods) structure solution programs and refined with the ShelXL-97[56] refinement package using least-squares minimization.

Energy Frameworks. CrystalExplorer 17.5[57] was used to calculate the aggregated pair-wise interaction energies and visualize the 3D topology energy frameworks of **1Me**, **1Et**, and **1nPr**. The energy calculations are accomplished on the B3LYP/6-31G** level of theory and by using crystal geometries (experimental structures), and the energy framework was constructed based on the crystal symmetry and the total intermolecular interaction energy of **1Me**, **1Et**, and **1nPr**. The energy components calculated within this method are electrostatic, polarization, dispersion, and exchange-repulsion and finally the total interaction energy (Table S2). The tube size, which is proportional to the intermolecular interaction energies used in all energy frameworks was 30, and the lower energy threshold (cut-off) value was set to zero. The aggregated total interaction energies along the stacks, tape, or slip layer direction were calculated by adding corresponding interaction energies between a given molecule in one layer and all interacting molecules in a neighboring layer or within the same layer within 3.8 Å (Figure S6, Supporting Information).

Nanoindentation. Nanoindentation tests were carried out using a TriboIndenter system (Hysitron Inc., Minneapolis, MN, USA) equipped with a Berkovich diamond tip with ∼100 nm radius. The indentations were performed in the load-controlled mode using a loading and unloading rate of 0.1 mN/s. For **1Et** and **1nPr** crystals, 25 indentations each were performed on different faces of at least 5 samples. A peak load, P_{max}, of 5 mN and a peak hold-time of 50 s were used. For **1Me**, P_{max} of 0.5 mN and a hold-time of 5 s were used; a relatively low load was applied here because of the softer nature of the crystal as well as to prevent overlap of indentation impressions with surface asperities that were present on these samples. The penetration depth, h_{max}, corresponding to P_{max} is found to be less than 10% of the sample thickness (which is more than 100, 80, and 120 μm for **1Me**, **1Et**, and **1nPr**, respectively) for all samples. This ensures that the substrate has had little or no effect on the measured load−depth, $P-h$, curves.[58] The indents were imaged using the in situ scanning probe microscopy capability of the Triboindenter system to examine the geometry of the impressions formed and the occurrence of material pileup, if any. The E and H values were obtained from the $P-h$ curves following the Oliver-Pharr procedure.[59,60] For precision in the estimation of E and H, the indenter tip was calibrated—prior to the indentation tests—on a fused quartz standard having an elastic modulus of 69.4 GPa.

Three-Point Bending Tests. Three-point bending tests were carried out using the high-load cell of the TriboIndenter system. Crystalline samples were placed on steel supports having an upper width of ∼70 μm. The supports were previously fixed onto a glass slide using cyanoacrylate glue, and the slide and support assembly was firmly positioned on the indenter stage at a magnetic location. A blunt spherical tip of ∼5 μm radius was used to load the simply supported crystalline beam at the center of its span length. A span length of 1 mm was chosen. A smaller span was found to indent the beam leading to a positive curvature in the measured load−deflection curve, whereas a larger span (for a given beam thickness) produced insubstantial strains in the beam. The choice of a blunt tip and a large span length ensured that there was no indentation during the bending test. The distance between the indenter and the optics was calibrated to ensure accurate positioning of the indenter tip at the desired location (center of width and span length) on the crystal for application of the bending load. All bending tests were carried out in the displacement controlled mode using a rate of 2 μm/s.

To ensure applicability of the simple beam bending theory and to minimize error in stiffness measurement, bending tests were carried out in the following configuration: (i) relatively large span length-to-thickness ratio ranging from 10 to 50, (ii) small deflection-to-span length ratio of less than 5, and (iii) estimated ratio of span length-to-support radius between 15 and 30.

Molecular crystals in the elastic region have been shown to undergo nearly pure bending even at large strains.[32−42] In the elastic limits, **1Et**, **1nPr**, and **1Me** are assumed to undergo bending with negligible shear deformation, and bending properties are calculated using the simple beam bending theory.[61,62] Using the beam deflection, measured through the depth sensing capability of the nanoindenter, the bending modulus, E_b, is calculated from the deflection equation as

$$E_b = \frac{PL^3}{48I\delta} \tag{1}$$

where P is the load applied at the center of the span length L, δ is the beam deflection at the center of span, and I is the area moment of inertia for a rectangular cross-section of width b. For a beam of thickness h, I is given by

$$I = \frac{bh^3}{12}$$

The maximum strain acting on the bottommost plane of the beam is calculated as

$$\epsilon_{max} = \frac{6\delta h}{L^2} \tag{2}$$

MD Simulations. *Full Atomistic Modeling.* Full atomistic MD simulations were performed using Large-scale Atomic/Molecular Massively Parallel Simulator.[63] The crystal structures (unit cell) of **1Me**, **1Et**, and **1nPr** used in the MD simulations were obtained from our SCXRD data. Because these NDIs are made of rigidly planar aromatic core groups, we adopted the consistent valence force field (CVFF)[64] in the MD simulations. The CVFF has been widely applied in modeling organic molecules with aromatic core groups such as benzene[65] and polydopamine.[66−68] The MD models of **1Me**, **1Et**, and **1nPr** were built by replicating the unit cells in [1 0 0], [0 1 0], and [0 0 1] directions several times. Periodic boundary conditions were applied, and the integration time step was set to 1.0 fs. The nonbonding interactions (12−6 Lennard-Jones and Coulombic interactions) were computed with a cutoff of 12 Å, and long-range interactions were calculated with a particle−particle particle-mesh solver. Energy minimization with the conjugate gradient algorithm was performed before MD equilibrations. In the first step, the MD models were equilibrated with the *NVT* ensemble at the initial temperature of 10 K increasing to the final temperature of 100 K for

DOI: 10.1021/acs.chemmater.8b04800
Chem. Mater. 2019, 31, 1391−1402

1.0 ns. In the second step, the MD models were equilibrated with the *NPT* ensemble at a constant temperature of 100 K and a pressure of 1.013 bar for 1.0 ns. In the final step, the MD models were equilibrated with the *NPT* ensemble at the initial temperature of 100 K increasing to the final temperature of 300 K and a pressure of 1.013 bar for 2.0 ns. The crystal sizes of **1Me**, **1Et**, and **1nPr** shown in Table 2 are calculated after the final step of MD equilibrations is finished.

Tensile and Shear Tests. The stresses of materials because of three-point bending tests can be decomposed into normal stress and shear stress. The normal stresses caused by pure bending can be calculated as

$$\sigma = \frac{My}{I}$$

where σ is the normal stress, M is the bending moment, y is the perpendicular distance to the neutral axis, and I is the area moment of inertia. The shear stress caused by shearing can be calculated as

$$\tau = \frac{VQ}{Ib}$$

where τ is the shear stresses, V is the shear force, Q is the first moment of area, I is the area moment of inertia, and b is the width of the beam.

From the above two equations, it is clear that the maximum normal stress occurs at both the top and bottom of the beam, where the shear stress is zero. On the other hand, the maximum shear stress occurs at the neutral axis of the beam, where the normal stress is zero. Thus, to simplify the problem, we performed tensile and shear tests separately. The tensile tests in the MD simulations were performed by applying tensile strains in the longitudinal direction [1 0 0] of the crystals to simulate the 3PF tests in our experiments when the force was applied on the (0 0 1) face of the crystal. A tensile strain of around 0.5% was applied to each of the MD model every 1.0 ns, and the corresponding tensile stress was measured with the *NPT* ensemble at a constant temperature of 300 K. Except the stretching direction, the pressures in the other two directions were set to 1.013 bar. As the force in the 3PF tests was applied on the (0 0 1) face of the crystal, the shear tests in the MD simulations were performed by applying shear strains in the [1 0 0]−[0 0 1] direction. A shear strain of around 1.0−1.5% was applied to each of the MD models every 1.0 ns, and the corresponding shear stress was measured with the *NPT* ensemble at a constant temperature of 300 K and a pressure of 1.013 bar. In the unloading tests, the MD models under different amounts of shear strain were equilibrated with the *NPT* ensemble at a constant temperature of 300 K and a pressure of 1.013 bar for 1.0 ns.

■ ASSOCIATED CONTENT

Supporting Information

The Supporting Information is available free of charge on the ACS Publications website at DOI: 10.1021/acs.chemmater.8b04800.

^{1}H NMR data, crystallographic information table, **1nPr** packing, π-stacking distances, energy frameworks, calculated aggregate total interaction energies of **1Me**, **1Et**, and **1nPr**, and intermolecular interaction energies of the three NDI derivatives (PDF)

■ AUTHOR INFORMATION

Corresponding Authors

*E-mail: mbuehler@mit.edu (M.J.B.).
*E-mail: ramu@iisc.ac.in (U.R.).
*E-mail: cmreddy@iiserkol.ac.in (C.M.R.).

ORCID

Chun-Teh Chen: 0000-0002-8645-4833
Bal Raju Kammari: 0000-0002-8144-0862
Markus J. Buehler: 0000-0002-4173-9659
C. Malla Reddy: 0000-0002-1247-7880

Present Addresses

#Department of Materials Science and Engineering, North Carolina State University, Raleigh, North Carolina 27695, USA (S.B.K.).
⊥CSIR-National Chemical Laboratory, Dr. Homi Bhabha Road, Pune 411 008, India (G.R.K.).

Author Contributions

The manuscript was written through contributions of all authors.

Notes

The authors declare no competing financial interest.

■ ACKNOWLEDGMENTS

C.M.R. acknowledges the financial support from the DST (DST/SJF/CSA-02/2014−15). R.D. and G.R.K. thank the IISER Kolkata for fellowship and instrumental facilities. K.B.R. thanks the DST-SERB, India, for the award of National Postdoctoral Fellowship (PDF/2015/000953). M.J.B. and C.T.C. acknowledge the support from ONR (N000141612333) and DOD-MURI (grant no. FA9550-15-1-0514).

■ REFERENCES

(1) Ruiz, C.; García-Frutos, E. M.; Hennrich, G.; Gómez-Lor, B. Organic Semiconductors toward Electronic Devices: High Mobility and Easy Processability. *J. Phys. Chem. Lett.* **2012**, *3*, 1428.
(2) Ghosh, S.; Reddy, C. M. Elastic and Bendable Caffeine Cocrystals: Implications for the Design of Flexible Organic Materials. *Angew. Chem., Int. Ed.* **2012**, *51*, 10319.
(3) Varughese, S.; Kiran, M. S. R. N.; Ramamurty, U.; Desiraju, G. R. Nanoindentation in Crystal Engineering: Quantifying Mechanical Properties of Molecular Crystals. *Angew. Chem., Int. Ed.* **2013**, *52*, 2701.
(4) Naumov, P.; Chizhik, S.; Panda, M. K.; Nath, N. K.; Boldyreva, E. Mechanically Responsive Molecular Crystals. *Chem. Rev.* **2015**, *115*, 12440.
(5) Zhu, L.; Al-Kaysi, R. O.; Bardeen, C. J. Photoinduced Ratchet-Like Rotational Motion of Branched Molecular Crystals. *Angew. Chem., Int. Ed.* **2016**, *55*, 7073.
(6) Hayashi, S.; Yamamoto, S.-y.; Takeuchi, D.; Ie, Y.; Takagi, K. Creating Elastic Organic Crystals of π-Conjugated Molecules with Bending Mechanofluorochromism and Flexible Optical Waveguide. *Angew. Chem., Int. Ed.* **2018**, *57*, 17002.
(7) Ahmed, E.; Karothu, D. P.; Naumov, P. Crystal Adaptronics: Mechanically Reconfigurable Elastic and Superelastic Molecular Crystals. *Angew. Chem., Int. Ed.* **2018**, *57*, 8837.
(8) Catalano, L.; Karothu, D. P.; Schramm, S.; Ahmed, E.; Rezgui, R.; Barber, T. J.; Famulari, A.; Naumov, P. Dual-Mode Light Transduction through a Plastically Bendable Organic Crystal as an Optical Waveguide. *Angew. Chem., Int. Ed.* **2018**, *57*, 17254.
(9) Hayash, S.; Koizumi, T.; Kamiya, N. Elastic Bending Flexibility of a Fluorescent Organic Single Crystal: New Aspects of the Commonly Used Building Block 4,7-Dibromo-2,1,3-benzothiadiazole. *Cryst. Growth Des.* **2017**, *17*, 6158.
(10) Huang, R.; Wang, C.; Wang, Y.; Zhang, H. Elastic Self-Doping Organic Single Crystals Exhibiting Flexible Optical Waveguide and Amplified Spontaneous Emission. *Adv. Mater.* **2018**, *30*, 1800814.
(11) Liu, H.; Bian, Z.; Cheng, Q.; Lan, L.; Wang, Y.; Zhang, H. Controllably Realizing Elastic/plastic Bending Based on a Room-temperature Posphorescent Waveguiding Organic Crystal. *Chem. Sci.* **2019**, *10*, 227.
(12) Owczarek, M.; Hujsak, A. K.; Ferris, D. P.; Prokofjevs, A.; Majerz, I.; Szklarz, P.; Zhang, H.; Sarjeant, A. A.; Stern, C. L.; Jakubas, R.; Hong, S.; Dravid, V. P.; Stoddart, J. F. Flexible Ferroelectric Organic Crystals. *Nat. Commun.* **2016**, *7*, 13108.

DOI: 10.1021/acs.chemmater.8b04800
Chem. Mater. 2019, 31, 1391−1402

(13) Wang, H.; Deng, L.; Tang, Q.; Tong, Y.; Liu, Y. Flexible Organic Single-Crystal Field-Effect Transistor for Ultra-Sensitivity Strain Sensing. *IEEE Electron Device Lett.* **2017**, *38*, 1598.
(14) Minemawari, H.; Yamada, T.; Matsui, H.; Tsutsumi, J. y.; Haas, S.; Chiba, R.; Kumai, R.; Hasegawa, T. Inkjet Printing of Single-Crystal Films. *Nature* **2011**, *475*, 364.
(15) Diao, Y.; Tee, B. C.-K.; Giri, G.; Xu, J.; Kim, D. H.; Becerril, H. A.; Stoltenberg, R. M.; Lee, T. H.; Xue, G.; Mannsfeld, S. C. B.; Bao, Z. Solution Coating of Large-Area Organic Semiconductor Thin Films with Aligned Single-Crystalline Domains. *Nat. Mater.* **2013**, *12*, 665.
(16) Alejandro, L. B.; Mannsfeld, C. B. S.; Ling, M. M.; Liu, S.; Tseng, R. J.; Reese, C.; Roberts, M. E.; Yang, Y.; Wudl, F.; Bao, Z. Patterning Organic Single-crystal Transistor Arrays. *Nature* **2006**, *444*, 913.
(17) Garcia-Frutos, E. M. Small Organic Single-Crystalline One-Dimensional Micro- And Nanostructures for Miniaturized Devices. *J. Mater. Chem. C* **2013**, *1*, 3633.
(18) Li, R.; Hu, W.; Liu, Y.; Zhu, D. Micro- and Nanocrystals of Organic Semiconductors. *Acc. Chem. Res.* **2010**, *43*, 529.
(19) Briseno, A. L.; Tseng, R. J.; Ling, M.-M.; Falcao, E. H. L.; Yang, Y.; Wudl, F.; Bao, Z. High-Performance Organic Single-Crystal Transistors on Flexible Substrates. *Adv. Mater.* **2006**, *18*, 2320.
(20) Gupta, S. K.; Jha, P.; Singh, A.; Chehimi, M. M.; Aswal, D. K. Flexible Organic Semiconductor Thin Films. *J. Mater. Chem. C* **2015**, *3*, 8468.
(21) Reddy, C. M.; Padmanabhan, K. A.; Desiraju, G. R. Structure–Property Correlations in Bending and Brittle Organic Crystals. *Cryst. Growth Des.* **2006**, *6*, 2720.
(22) Krishna, G. R.; Devarapalli, R.; Lal, G.; Reddy, C. M. Mechanically Flexible Organic Crystals Achieved by Introducing Weak Interactions in Structure: Supramolecular Shape Synthons. *J. Am. Chem. Soc.* **2016**, *138*, 13561.
(23) Garai, M.; Santra, R.; Biradha, K. Tunable Plastic Films of a Crystalline Polymer by Single-Crystal-to-Single-Crystal Photopolymerization of a Diene: Self-Templating and Shock-Absorbing Two-Dimensional Hydrogen-Bonding Layers. *Angew. Chem., Int. Ed.* **2013**, *52*, 5548.
(24) Day, G. M.; Price, S. L.; Leslie, M. Elastic Constant Calculations for Molecular Organic Crystals. *Cryst. Growth Des.* **2001**, *1*, 13.
(25) West, A. R. *Solid State Chemistry and its Applications*; Wiley: Chichester, U.K., 1984.
(26) Pavlides, P.; Pugh, D.; Roberts, K. J. Elastic-Tensor Atom-Atom Potential Calculations for Molecular Crystals: C_6H_6 and $CO(NH_2)_2$. *Acta Crystallogr.* **1991**, *47*, 846.
(27) Sherwood, J. N. *Plastically Crystalline State: Orientationally Disordered Crystals*; Wiley: Chichester [Eng.]; New York, 1979.
(28) Reddy, C. M.; Rama Krishna, G.; Ghosh, S. Mechanical Properties of Molecular Crystals—Applications to Crystal Engineering. *CrystEngComm* **2010**, *12*, 2296.
(29) Reddy, C. M.; Basavoju, S.; Desiraju, G. R. Sorting of Polymorphs Based on Mechanical Properties. Trimorphs of 6-chloro-2,4-dinitroaniline. *Chem. Commun.* **2005**, 2439.
(30) Reddy, C. M.; Gundakaram, R. C.; Basavoju, S.; Kirchner, M. T.; Padmanabhan, K. A.; Desiraju, G. R. Structural Basis for Bending of Organic Crystals. *Chem. Commun.* **2005**, 3945.
(31) Panda, M. K.; Ghosh, S.; Yasuda, N.; Moriwaki, T.; Mukherjee, G. D.; Reddy, C. M.; Naumov, P. Spatially Resolved Analysis of Short-Range Structure Perturbations in a Plastically Bent Molecular Crystal. *Nat. Chem.* **2014**, *7*, 65.
(32) Đaković, M.; Borovina, M.; Pisačić, M.; Aakeröy, C. B.; Soldin, Ž.; Kukove, B. M.; Kodrin, I. Mechanically Responsive Crystalline Coordination Polymers with Controllable Elasticity. *Angew. Chem., Int. Ed.* **2018**, *57*, 14801.
(33) Raju, K. B.; Ranjan, S.; Vishnu, V. S.; Bhattacharya, M.; Bhattacharya, B.; Mukhopadhyay, A. K.; Reddy, C. M. Rationalizing Distinct Mechanical Properties of Three Polymorphs of a Drug Adduct by Nanoindentation and Energy Frameworks Analysis: Role of Slip Layer Topology and Weak Interactions. *Cryst. Growth Des.* **2018**, *18*, 3927.
(34) Ghosh, S.; Mishra, M. K.; Kadambi, S. B.; Ramamurty, U.; Desiraju, G. R. Designing Elastic Organic Crystals: Highly Flexible Polyhalogenated N-Benzylideneanilines. *Angew. Chem., Int. Ed.* **2015**, *54*, 2674.
(35) Hayashi, S.; Koizumi, T. Elastic Organic Crystals of a Fluorescent π-Conjugated Molecule. *Angew. Chem., Int. Ed.* **2016**, *55*, 2701.
(36) Chou, C.-M.; Nobusue, S.; Saito, S.; Inoue, D.; Hashizume, D.; Yamaguchi, S. Highly Bent Crystals Formed by Restrained Π-Stacked Columns Connected via Alkylene Linkers with Variable Conformations. *Chem. Sci.* **2015**, *6*, 2354.
(37) Medishetty, R.; Sahoo, S. C.; Mulijanto, C. E.; Naumov, P.; Vittal, J. J. Photosalient Behavior of Photoreactive Crystals. *Chem. Mater.* **2015**, *27*, 1821.
(38) Liu, H.; Lu, Z.; Zhang, Z.; Wang, Y.; Zhang, H. Highly Elastic Organic Crystals for Flexible Optical Waveguides. *Angew. Chem.* **2018**, *130*, 8584.
(39) Chattoraj, S.; Shi, L.; Sun, C. C. Understanding the Relationship Between Crystal Structure, Plasticity and Compaction Behaviour of Theophylline, Methyl Gallate, and their 1:1 Co-crystal. *CrystEngComm* **2010**, *12*, 2466.
(40) Krishna, G. R.; Shi, L.; Bag, P. P.; Sun, C. C.; Reddy, C. M. Correlation among Crystal Structure, Mechanical Behavior, and Tabletability in the Co-Crystals of Vanillin Isomers. *Cryst. Growth Des.* **2015**, *15*, 1827.
(41) Liu, F.; Hooks, D. E.; Li, N.; Mara, N. A.; Swift, J. A. Mechanical Properties of Anhydrous and Hydrated Uric Acid Crystals. *Chem. Mater.* **2018**, *30*, 3798.
(42) Rupasinghe, T. P.; Hutchins, K. M.; Bandaranayake, B. S.; Ghorai, S.; Karunatilake, C.; Bučar, D.-K.; Swenson, D. C.; Arnold, M. A.; MacGillivray, L. R.; Tivanski, A. V. Mechanical Properties of a Series of Macro- and Nanodimensional Organic Cocrystals Correlate with Atomic Polarizability. *J. Am. Chem. Soc.* **2015**, *137*, 12768.
(43) Molla, M. R.; Das, A.; Ghosh, S. Self-Sorted Assembly in a Mixture of Donor and Acceptor Chromophores. *Chem.—Eur. J.* **2010**, *16*, 10084.
(44) Mukherjee, A.; Desiraju, G. R. Halogen Bonds in Some Dihalogenated Phenols: Applications to Crystal Engineering. *IUCrJ* **2013**, *1*, 49.
(45) Worthy, A.; Grosjean, A.; Pfrunder, MC; Xu, Y.; Yan, C.; Edwards, G.; Clegg, JK; McMurtrie, JC Atomic Resolution of Structural Changes in Elastic Crystals of Copper(II)Acetylacetonate. *Nat Chem* **2018**, *10*, 65–69.
(46) Kahr, B.; Ward, MD Flexible Molecular Materials: Stressed out Crystals. *Nat Chem* **2017**, *10*, 4–6.
(47) Takamizawa, S.; Miyamoto, Y. Superelastic Organic Crystals. *Angew. Chem., Int. Ed.* **2014**, *53*, 6970.
(48) Takamizawa, S.; Takasaki, Y. Superelastic Shape Recovery of Mechanically Twinned 3,5-Difluorobenzoic Acid Crystals. *Angew. Chem., Int. Ed.* **2015**, *54*, 4815.
(49) Turner, M. J.; Thomas, S. P.; Shi, M. W.; Jayatilaka, D.; Spackman, M. A. Energy frameworks: insights into interaction anisotropy and the mechanical properties of molecular crystals. *Chem. Commun.* **2015**, *51*, 3735.
(50) Thomas, S. P.; Shi, M. W.; Koutsantonis, G. A.; Jayatilaka, D.; Edwards, A. J.; Spackman, M. A. The Elusive Structural Origin of Plastic Bending in Dimethyl Sulfone Crystals with Quasi-isotropic Crystal Packing. *Angew. Chem. Int. Ed.* **2017**, *56*, 8468.
(51) Mackenzie, C. F.; Spackman, P. R.; Jayatilaka, D.; Spackman, M. A. CrystalExplorer model energies and energy frameworks: extension to metal coordination compounds, organic salts, solvates and open-shell systems. *IUCrJ* **2017**, *4*, 575.
(52) Chang, L.; Zhang, L. C. Deformation Mechanisms at Pop-Out in Monocrystalline Silicon under Nanoindentation. *Acta Mater.* **2009**, *57*, 2148.

DOI: 10.1021/acs.chemmater.8b04800
Chem. Mater. 2019, 31, 1391–1402

(53) Caër, C.; Patoor, E.; Berbenni, S.; Lecomte, J.-S. Stress Induced Pop-In and Pop-Out Nanoindentation Events in CuAlBe Shape Memory Alloys. *Mater. Sci. Eng., A* **2013**, *587*, 304.
(54) Beer, F. P.; Johnston, E. R.; Dewolf, J. T. *Mechanics of Materials*, 3rd ed.; McGraw-Hill Book Company: New York, 2002.
(55) Dolomanov, O. V.; Bourhis, L. J.; Gildea, R. J.; Howard, J. A. K.; Puschmann, H. OLEX2: A Complete Structure Solution, Refinement and Analysis Program. *J. Appl. Crystallogr.* **2009**, *42*, 339.
(56) Sheldrick, G. M. *SHELXS97 and SHELXL97. Program for Crystal Structure Solution and Refinement*; University of Göttingen: Göttingen, 1997.
(57) Turner, M. J.; Grabowsky, S.; Jayatilaka, D.; Spackman, M. A. Accurate and Efficient Model Energies for Exploring Intermolecular Interactions in Molecular Crystals. *J. Phys. Chem. Lett.* **2014**, *5*, 4249.
(58) Ramamurty, U.; Jang, J.-i. Nanoindentation for Probing the Mechanical Behavior of Molecular Crystals—A Review of the Technique and How to use it. *CrystEngComm* **2014**, *16*, 12.
(59) Oliver, W. C.; Pharr, G. M. An Improved Technique for Determining Hardness and Elastic Modulus Using Load and Displacement Sensing Indentation Experiments. *J. Mater. Res.* **2011**, *7*, 1564.
(60) Oliver, W. C.; Pharr, G. M. Measurement of Hardness and Elastic Modulus by Instrumented Indentation: Advances in Understanding and Refinements to Methodology. *J. Mater. Res.* **2004**, *19*, 3.
(61) Bauchau, O. A.; Craig, J. I. Euler-Bernoulli Beam Theory. *Structural Analysis*; Springer: Netherlands, 2009; p 173.
(62) Timoshenko, S. *Strength of Materials: Part I (Elementary Theory and Problems)*, 3rd ed.; Robert E. Krieger Publishing Co.: Huntington, 1976.
(63) Plimpton, S. Fast Parallel Algorithms for Short-Range Molecular Dynamics. *J. Comp. Physiol.* **1995**, *117*, 1.
(64) Dauber-Osguthorpe, P.; Roberts, V. A.; Osguthorpe, D. J.; Wolff, J.; Genest, M.; Hagler, A. T. Structure and Energetics of Ligand Binding to Proteins: Escherichia Coli Dihydrofolate Reductase-Trimethoprim, A Drug-Receptor System. *Proteins: Struct., Funct., Genet.* **1988**, *4*, 31.
(65) Hou, T. J.; Zhu, L. L.; Xu, X. J. Adsorption and Diffusion of Benzene in ITQ-1 Type Zeolite: Grand Canonical Monte Carlo and Molecular Dynamics Simulation Study. *J. Phys. Chem. B* **2000**, *104*, 9356.
(66) Chen, C.-T.; Ball, V.; de Almeida Gracio, J. J.; Singh, M. K.; Toniazzo, V.; Ruch, D.; Buehler, M. J. Self-Assembly of Tetramers of 5,6-Dihydroxyindole Explains the Primary Physical Properties of Eumelanin: Experiment, Simulation, and Design. *ACS Nano* **2013**, *7*, 1524.
(67) Chen, C.-T.; Chuang, C.; Cao, J.; Ball, V.; Ruch, D.; Buehler, J. M. Excitonic Effects from Geometric Order and Disorder Explain Broadband Optical Absorption in Eumelanin. *Nat. Commun.* **2014**, *5*, 3859.
(68) Chen, C.-T.; Ghosh, S.; Malla Reddy, C.; Buehler, M. J. Molecular Mechanics of Elastic and Bendable Caffeine Co-Crystals. *Phys. Chem. Chem. Phys.* **2014**, *16*, 13165.

DOI: 10.1021/acs.chemmater.8b04800
Chem. Mater. 2019, 31, 1391−1402